AIAA 2003–3237

AERO ACOUSTIC INVESTIGATION OF AN OPEN CAVITY AT LOW MACH NUMBER

Johan Larsson
Volvo Car Corporation, Göteborg, Sweden
Lars Davidson
Chalmers University of Technology, Göteborg, Sweden
Magnus Olsson
Volvo Car Corporation, Göteborg, Sweden
Lars-Erik Eriksson
Chalmers University of Technology, Göteborg, Sweden

9th AIAA/CEAS Aeroacoustics Conference and Exhibit
May 12–14, 2003 / Hilton Head, SC

AERO ACOUSTIC INVESTIGATION OF AN OPEN CAVITY AT LOW MACH NUMBER

Johan Larsson*
Volvo Car Corporation, Göteborg, Sweden
Lars Davidson†
Chalmers University of Technology, Göteborg, Sweden
Magnus Olsson‡
Volvo Car Corporation, Göteborg, Sweden
Lars-Erik Eriksson§
Chalmers University of Technology, Göteborg, Sweden

The laminar flow and the near-field acoustics of an open cavity at Mach number 0.15 is computed by direct solution (two-dimensional) of the compressible Navier-Stokes equations. A modified version of Curle's equation, that is suitable for numerical computations and valid in the near-field, is derived. The radiated sound computed by the modified Curle's equation is compared to the directly computed sound field, and the agreement is found to be good.

The contributions from the various source terms in Curle's equation are quantified, and the terms involving wall pressure fluctuations are found to account for approximately 90% of the radiated intensity. These main source terms are investigated further, and it is found that they are especially large in the downstream part of the cavity, and for about two cavity lengths downstream of the cavity. The upstream dominance of the radiated sound is explained by the fact that the downstream cavity wall contributes primarily to the upstream direction. Correlations between the radiated sound and the source terms show that the near-field terms display a stronger directivity than the far-field terms, and hence the far-field directivity will be flatter.

1 Introduction

AERO acoustics, or the sound generated by fluid flows, is an area of research which has received an increasing amount of attention during the last decade. Most of the research has been aimed at high Mach number applications, with jet noise being the most typical case of interest. With the increases in performance of computers, the numerical simulation of aero acoustics, or Computational Aero Acoustic (CAA), has become more popular.

The interest for aero acoustics in the vehicle industry has increased during the last few years, primarily due to customer surveys that show wind noise to be a common complaint. In vehicle applications, the Mach numbers of the flows are typically small, and the flows are often heavily separated due to the complex geometries present.

The motion in a compressible fluid is determined by the governing equations, together with proper boundary conditions. While being a trivial remark, this means that the acoustics and the flow are intrinsically coupled, and it is, on a philosophical level, not possible to think of acoustics and flow as two separate phenomena. For many cases, however, it is possible to split the problem in two parts: the fluid flow problem, and the acoustic problem. If the problem can be split, there are two main approaches to describe the acoustic part of the problem: by a scalar equation, or by a system of equations. In this work, the scalar equation approach is chosen, since an analytical solution for the radiated sound field is sought.

The scalar equations were pioneered by Lighthill[1] who, by rewriting the governing equations, derived

$$\frac{\partial^2 \rho}{\partial t^2} - a_\infty^2 \frac{\partial^2 \rho}{\partial x_i^2} = \frac{\partial^2 T_{ij}}{\partial x_i \partial x_j} \qquad (1)$$

where $T_{ij} = \rho u_i u_j - \tau_{ij} + (p - a_\infty^2 \rho)\delta_{ij}$ and a_∞ is the ambient speed of sound. Equation (1) can be viewed as a wave equation for the propagation of sound. Several others have proposed scalar wave equations hence. Among others, the contributions by Phillips,[2] Lilley,[3] and Doak[4] can be mentioned. Curle[5] solved Lighthill's equation on a bounded domain, and Ffowcs Williams and Hawkings[6] extended Curle's solution to include surfaces in motion. The present work focuses on problems involving solid surfaces, but where the surfaces

---

[*] PhD student: njlarsso@sunwise.uwaterloo.ca

[†] Professor, supervisor: lada@tfd.chalmers.se

[‡] Dr.

[§] Professor.

are stationary relative to the observer. For such problems, the solutions by Curle and Ffowcs Williams and Hawkings are equivalent, and it is matter of preference which one to use. Here, Curle's equation will be used.

When working with the scalar acoustic equations, it is vital to understand the assumptions introduced. In the case of Lighthill's equation, no assumptions have been made in the derivation, and hence it is exact. When solving Lighthill's equation analytically, however, it is *implicitly* assumed that the source terms do not depend on the acoustic field, and that the isotropic wave operator describes the propagation of sound correctly. Mathematically speaking, the first assumption is *never* true, since the density appears on both sides of the equation, as pointed out by for example Doak.[4] Physically speaking, it can be argued that the first assumption is a valid one (i.e. that it introduces only small errors) when the sound is generated by hydrodynamic phenomena, which are almost independent of the acoustic field. The second assumption is true only in regions where the fluid is stagnant, i.e. zero. In low Mach number flows, the second assumption is expected to be a good approximation, since convection effects are a factor M slower than the propagation of the acoustic waves. A more thorough discussion can be found in Larsson.[7]

When computing the solution to Lighthill's equation numerically, Sarkar and Hussaini[8] argued that it is favourable to transform the spatial derivatives to temporal ones. The reason is that the temporal form of the solution is less sensitive to numerical errors. Sarkar and Hussaini's temporal form of the solution is, however, only valid in the far field, since this approximation was introduced in their derivation. In the current work, the sound in the near field is of interest, and hence Sarkar and Hussaini's form of the solution is not valid. Therefore, a new form of Curle's solution to Lighthill's equation will be derived.

1.1 Objectives

The objectives of the present work is to:

- Investigate the noise generation process, specifically the noise generation in wall bounded, separated, low Mach number flows.
- Derive a form of the solution to Lighthill's equation that is suitable for computational applications and valid in both the near and far fields.
- Quantify the importance of the sound sources existing in the fluid, compared to that of the sources existing on solid walls.

1.2 Open Cavity

The test case chosen in this study is the *open cavity*, which has been investigated theoretically, experimentally, and computationally, by many researchers. While making no attempt at reviewing all the work that has been done on the open cavity, included here is some work that is relevant to the current work.

Gharib and Roshko[9] studied the incompressible flow in and around axisymmetric cavities experimentally, and found that the flow in a cavity is heavily dependent on the length to depth (L/D) ratio. At low L/D, a shear layer is formed along the upper part of the cavity. The flow above the cavity is relatively undisturbed, and the main unsteady flow feature is the convection of vortices in the shear layer. The drag of the cavity is fairly low, typically $C_D \sim 0.01$. At higher L/D, the flow becomes more violent and unsteady. A vortex that fills the whole cavity is formed at the leading edge of the cavity, and when it is large enough it is released at the trailing edge. The flow above the cavity is affected by the flow inside the cavity, and freestream fluid is periodically directed into the cavity. The drag in this flow regime is much higher, typically $C_D \sim 0.3$. Gharib and Roshko used the term *wake-mode* to describe this latter flow regime, and some researchers use the term *shear-mode* to describe the first one. Here, the terms *shear regime* and *wake regime* will be used, in order to avoid confusion with the term *mode*, which is used for dominant frequencies.

The review of Rockwell and Naudascher[10] offers an excellent overview of the various types of cavity flows, and of what parameters are important in determining the character of the flow. Included in this review are the measurements and findings by Ethembabaoglu,[11] Sarohia,[12] and Rossiter.[13] Ethembabaoglu performed incompressible experiments with turbulent boundary layers, and found that the spectrums of the wall pressure fluctuations were highly organized with clear peaks. This suggests that a feedback mechanism is present, which couples the flow and the acoustics in a two-way manner (the feedback mechanism will be explained at the end of this section), and that the turbulence itself may be of secondary importance to the oscillations. In experiments with laminar boundary layers, Sarohia found that the cavity depth is insignificant, unless it is of the same order of magnitude as the boundary layer thickness $\delta_{0.99}$. Rossiter stressed the importance of the boundary layer upstream of the cavity, and found that a thinner boundary layer generates larger levels of fluctuations in the cavity.

Ahuja and Mendoza[14] performed aero acoustic measurements in cavities with the purpose of using the results for validation of CAA codes. Among other things, they studied the importance of $\delta_{0.99}$, L/D ratio, the influence of the spanwise width of the cavity, and the Mach number, on the radiated sound in several directions.

During especially the last couple of years, several numerical studies of open cavity flows have been published. Colonius *et al*[15] performed Direct Simulations of the flow in 2D cavities at fairly low Reynolds numbers, typically $Re_D = 1500$. Varying several parameters, including L/D, M, and $\delta_{0.99}$, they found that the primary parameter deciding which flow regime (shear or wake regime) that will be present, is L/θ, where θ is the momentum thickness of the boundary layer.

Shieh and Morris[16] performed Large Scale Simulations (LSS) of cavities with $L/D = 2$ and $L/D = 4.4$ at Mach numbers 0.4, 0.5, and 0.6. Their presented Reynolds number is 200000, but is unclear from their paper what dimension this is based on. They found that the mean streamlines in the shear regime are virtually undisturbed above the cavity, but clearly not so in the wake regime. Also, they found the mean pressure profiles along the bottom of the cavity to be distinctly different between the shear and wake regimes.

Ashcroft and Zhang[17] repeated Ahuja and Mendoza's measurements using Unsteady RANS (URANS), and captured the main flow features. This is yet another indication that it is the feedback mechanisms of the low-frequency modes that are controlling the cavity flow.

Many attempts at deriving feedback models that predict the dominant frequencies have been made, with Rossiter's[13] being the first one. These models typically try to model the convection of a vortex in the shear layer, the impingement of this vortex on the downstream cavity wall, the propagation upstream of an acoustic wave, and the triggering of a new vortex near the leading edge. These models are typically fairly successful in predicting shear regime flows, but rather unsuccessful in predicting wake regime flows. This comes as no surprise, since the feedback mechanism modeled only applies to the shear regime. The current focus of feedback modeling seems to be to find the criterion for the regime-switching. Rossiter's model is

$$St_L = \frac{fL}{U_\infty} = \frac{m-\phi}{M+\frac{1}{\kappa}} \tag{2}$$

where f is the frequency, m is the mode number (integer), ϕ is the phase-lag between vortex impingement and emission of sound at the downstream wall, and κ is the ratio of the eddy convection velocity to the freestream velocity.

The case studied in the current work has a length to depth ratio of $L/D = 4$, a Mach number of $M = 0.15$, and a Reynolds number of $Re_D = 1500$. At this Reynolds number, the flow is laminar, and hence the simulation is performed in two dimensions.

Since no experimental or computational data exists for this particular case, a Direct Simulation (DS) that resolves both the flow and the acoustics is performed. The term Direct Simulation is used here to avoid confusion with Direct Numerical Simulation, a term normally used for the simulation of turbulence. The DS will be used to compute the source terms in Curle's integral solution, and will be used for the purpose of comparisons.

2 Methodology, Direct Simulation

The code used for the Direct Simulation is based on the finite volume code written by Eriksson.[18] Versions of this code has previously been used to study jet noise[19] and the sound emitted from shear layers.[20] Several modifications were made, including increasing the spatial and temporal accuracy, making the code work in 2D, and making the code parallel by the use of Message Passing Interface (MPI). The modifications are described in greater detail in Larsson.[7]

2.1 Governing Equations

The compressible Navier-Stokes equations, written on a compact, conservative form, are

$$\frac{\partial Q}{\partial t} + \frac{\partial E_j}{\partial x_j} = \frac{\partial F_j}{\partial x_j} \tag{3}$$

where $Q = (\rho, \rho u_i, \rho e_o)^T$ is the state vector, $E_j = (\rho u_j, \rho u_i u_j + p\delta_{ij}, \rho e_o u_j + p u_j)^T$ is the inviscid fluxes, and $F_j = (0, \tau_{ij}, \tau_{ij} u_i - q_j)^T$ is the diffusive fluxes. The viscous stress tensor is

$$\tau_{ij} = \mu\left(\frac{\partial u_i}{\partial x_j} + \frac{\partial u_j}{\partial x_i} - \frac{2}{3}\frac{\partial u_k}{\partial x_k}\delta_{ij}\right) \tag{4}$$

and the heat flux q_i is modeled by Fourier's heat law

$$q_i = -\frac{c_p \mu}{Pr}\frac{\partial T}{\partial x_i} \tag{5}$$

where c_p is the specific heat at constant pressure. $e_o = e + u_i u_i/2$ is the total energy.

2.2 Numerical Scheme

The governing equations are discretized using the finite volume method. The inviscid fluxes are computed by the Dispersion Relation Preserving (DRP) scheme of Tam and Webb,[21] where a 6th order artificial dissipation term has been added for stability. The viscous fluxes, being orders of magnitude smaller than the inviscid ones, and less important for the acoustics, are computed by a 2nd order accurate, central scheme. The solution is stepped in time using a 4th order accurate, 4-stage Runge-Kutta method.

The boundary conditions are based on the characteristic variables at the boundary. These boundary conditions are non-reflective only for disturbances normal to the boundary, but have been reported[22] to be robust for problems where large non-linear fluctuations (vortices) have to leave the domain. To minimize the reflections from the boundaries, buffer layers, where the solution is slowly damped towards its boundary state, have been added. In the buffer layers, equation (3) is replaced by

$$\frac{\partial Q}{\partial t} + \frac{\partial E_j}{\partial x_j} = \frac{\partial F_j}{\partial x_j} - \sigma_o \xi^2 (Q - Q^*) \tag{6}$$

where σ_o is a buffer parameter, ξ is the non-dimensional distance from the beginning of the buffer layer ($0 \leq \xi \leq 1$), and Q^* is the target state.

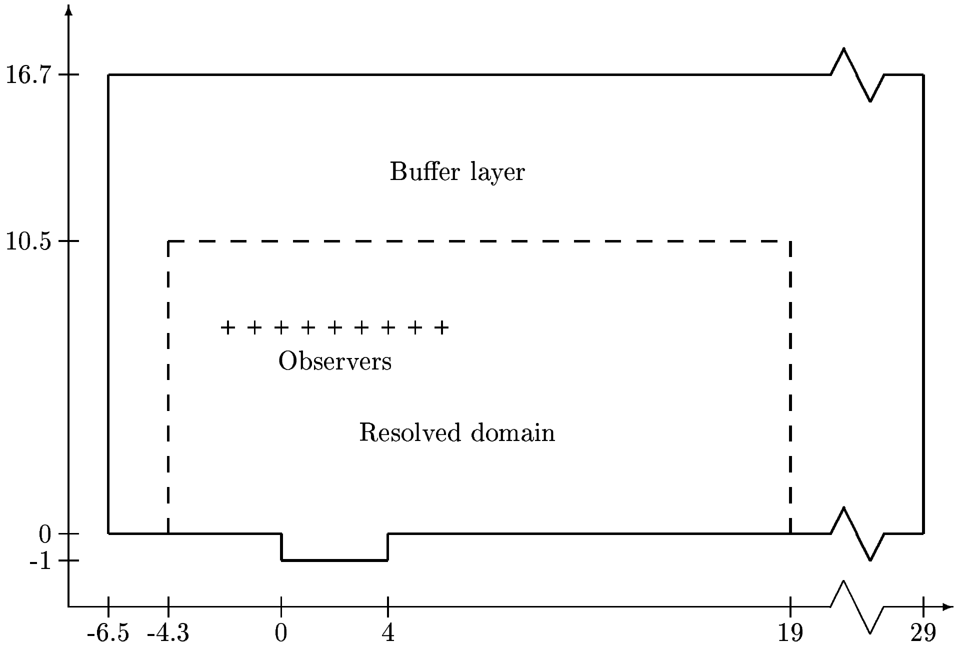

Fig. 1 Computational domain, coordinates normalized by D

2.3 Computational Grid

The computational domain is shown in figure 1, where the flow is from left to right. The resolution is roughly 80 cells per unit length (D) in and around the cavity, and the grid is stretched less than 1% per cell in the whole resolved domain. An upper limit on the cell size (roughly 3 times the smallest cell size) is set to avoid acoustic waves being reflected in the grid; if a high wavenumber wave reaches a region where the cell size is too large for it to be resolved, it will be reflected *in the grid* and contaminate the solution. The resolved domain extends between $-4.3 \leq x_1/D \leq 19$, and for $x_2/D \leq 10.5$. The total number of cells is 593900, of which 122700 are located in the buffer layers.

2.4 Grid Independence

Grid independence studies are important in all areas of CFD, and especially so in Direct Simulations of sound. The resolution has to be fine enough to resolve all important physics, and the boundary conditions must not affect the solution significantly. The latter is critical in CAA, since sound waves propagate over large distances. Although a boundary may be far away from the region of interest, any reflected sound waves will contaminate the solution in the *whole* domain.

The shortest wavelength of interest is $\lambda_{min}/D = (L/D)/(MSt_L) \approx 7$, since most of the energy is contained in $St_L \leq 4$. At this wavelength, the resolution is roughly 500 cells per wavelength, which indicates that the resolution is, indeed, fine.

The influence of the locations of the boundaries is tested by a simulation using a similar grid in and around the cavity, but with the boundaries moved closer to the cavity. The downstream boundary is moved $5D$ to $x_1/D = 14$, and the freestream boundary is moved $1.7D$ to $x_2/D = 8.8$. The lengths of the buffer layers are kept constant. The upstream boundary is kept, since it, and the buffer layer, determines the incoming boundary layer thickness.

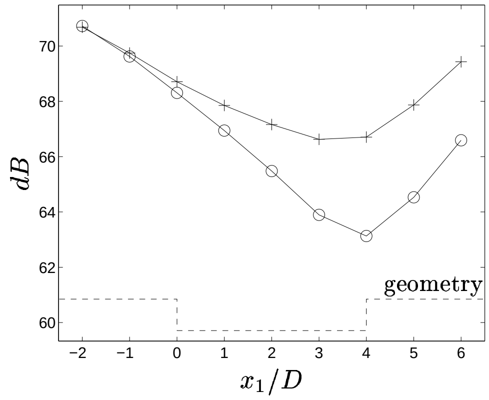

Fig. 2 Grid independence, OASPL. 'o' standard grid, '+' shortened grid

The main parameters St_L, $\overline{C}_D$, and $\overline{C}_D^p$ are completely unaffected, which is encouraging but expected. The real test is the sound at the observer locations (shown in figure 1), since the boundary conditions may reflect or generate sound that would contaminate the sound at those (or any other) positions. The Overall Sound Pressure Level (OASPL) is computed for both the standard grid and the shortened one, and plotted in figure 2. The two grids give similar OASPL at the upstream locations, but the shorter grid gives larger values at all other locations, especially the ones downstream. The largest difference is 3.6 dB. To further analyze the differences, the pressure signals at locations 1 ($x_1/D = -2$) and 7 ($x_1/D = 4$) are plotted in

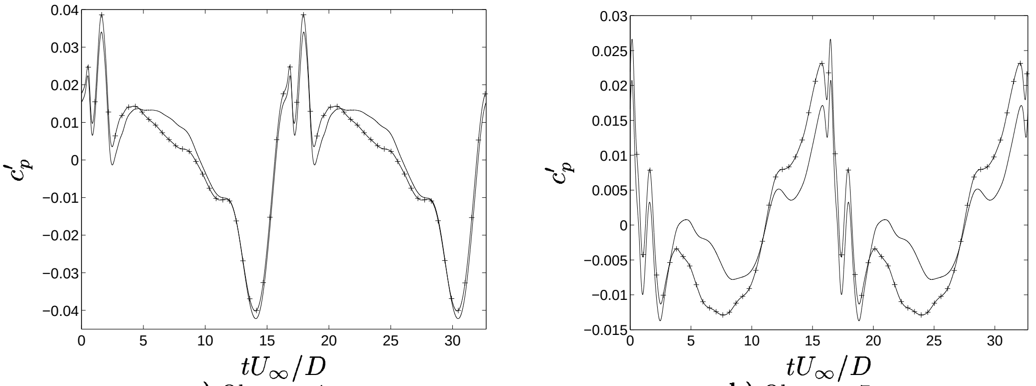

a) Observer 1 **b)** Observer 7

Fig. 3 Grid independence, p' versus time. '-' standard grid, '-+' shortened grid

figure 3, since these positions show the best (observer 1) and the worst (observer 7) grid independence in figure 2, respectively. The pressure signal at location 1 has changed slightly, but the main peaks are still correct. The signal at location 7 has changed more. While the peaks are still captured, small differences in levels and phase are present.

Can the solution be considered independent of the grid? Qualitatively speaking, the different grids give similar results, but the quantitative differences are fairly large. In this study, the database generated with the standard grid is considered reasonably grid independent, but the errors found here should be kept in mind when analyzing the results later on. The error in the standard grid is estimated to be smaller than the difference in $OASPL$ between the standard and the shortened grids, which yields an estimated maximum error of 3.6 dB.

In terms of future work, a real study on the boundary condition dependence is clearly of high priority.

3 Methodology, Curle's Equation

Curle[5] wrote the solution to Lighthill's equation as

$$\rho(\mathbf{x},t) - \rho_o = \frac{1}{4\pi a_\infty^2}\frac{\partial^2}{\partial x_i \partial x_j}\int_V \frac{T_{ij}}{r} dV(\mathbf{y}) - \frac{1}{4\pi a_\infty^2}\frac{\partial}{\partial x_i}\int_S \frac{n_j}{r}\left(p\delta_{ij} - \tau_{ij}\right) dS(\mathbf{y}) \tag{7}$$

where ρ_o is a constant of integration, $r = |\mathbf{x} - \mathbf{y}|$ is the distance between the source and the observer, and n_j is the surface normal pointing towards the fluid. The integrands are to be evaluated at the retarded time $\tau = t - r/a_\infty$

3.1 Modified Curle's Equation

Curle's equation (7) is on a form with the spatial derivatives outside the integral, but for numerical computations, it is better to have the derivatives inside the integral. This, together with Sarkar and Hussaini's[8] arguments that temporal derivatives of the source terms are preferable over spatial derivatives, suggests that equation (7) should be modified along those lines. In this work, the radiated sound fairly close to the region of generation is to be studied, and hence Sarkar and Hussaini's assumption that r is much larger than the extent of the sources is invalid. This assumption, however, is not necessary, and will not be used here.

If the observer in equation (7) is located in a region where the flow is isentropic, the density fluctuation at this location can be written $\rho(\mathbf{x},t) - \rho_o = (p(\mathbf{x},t) - p_o)/a_\infty^2$. For a function $f(\tau)$ the spatial derivative can be converted to a temporal one by

$$\frac{\partial f(\tau)}{\partial x_i} = \frac{\partial f}{\partial \tau}\frac{\partial \tau}{\partial x_i} = -\frac{1}{a_\infty}\frac{\partial r}{\partial x_i}\frac{\partial f}{\partial \tau} \tag{8}$$

The $\partial r/\partial x_i$ term becomes

$$\frac{\partial r}{\partial x_i} = \frac{\partial\sqrt{(x_j - y_j)^2}}{\partial x_i} = \frac{(x_i - y_i)}{\sqrt{(x_j - y_j)^2}} = \frac{x_i - y_i}{r} = l_i \tag{9}$$

where l_i is a unit vector pointing from the source location to the observer location. Using this, equation (7) can be written as

$$\begin{aligned} p(\mathbf{x},t) - p_o &= \\ &= \frac{1}{4\pi}\frac{\partial}{\partial x_i}\int_V -l_j\left[\frac{\dot{T}_{ij}}{a_\infty r} + \frac{T_{ij}}{r^2}\right] dV(\mathbf{y}) \\ &\quad -\frac{1}{4\pi}\int_S -l_i n_j\left[\frac{\dot{p}\delta_{ij} - \dot{\tau}_{ij}}{a_\infty r} + \frac{p\delta_{ij} - \tau_{ij}}{r^2}\right] dS(\mathbf{y}) \\ &= \frac{1}{4\pi}\int_V \left(l_i l_j\left[\frac{\ddot{T}_{ij}}{a_\infty^2 r} + 2\frac{\dot{T}_{ij}}{a_\infty r^2} + 2\frac{T_{ij}}{r^3}\right] \right. \\ &\quad \left. -\frac{\partial l_j}{\partial x_i}\left[\frac{\dot{T}_{ij}}{a_\infty r} + \frac{T_{ij}}{r^2}\right]\right) dV(\mathbf{y}) \\ &\quad +\frac{1}{4\pi}\int_S l_i n_j\left[\frac{\dot{p}\delta_{ij} - \dot{\tau}_{ij}}{a_\infty r} + \frac{p\delta_{ij} - \tau_{ij}}{r^2}\right] dS(\mathbf{y}) \end{aligned} \tag{10}$$

The term $\partial l_j / \partial x_i$ is expanded to

$$\frac{\partial l_j}{\partial x_i} = \frac{\partial}{\partial x_i}\left[\frac{x_j - y_j}{r}\right] = \frac{\delta_{ij} - l_i l_j}{r} \tag{11}$$

Inserting this into equation (10) yields

$$\begin{aligned} p(\mathbf{x},t) - p_o &= \\ &= \frac{1}{4\pi}\int\limits_V \left[\frac{l_i l_j}{a_\infty^2 r}\ddot{T}_{ij} + \frac{3 l_i l_j - \delta_{ij}}{a_\infty r^2}\dot{T}_{ij} \right. \\ &\qquad \left. + \frac{3 l_i l_j - \delta_{ij}}{r^3} T_{ij}\right] dV(\mathbf{y}) \\ &+ \frac{1}{4\pi}\int\limits_S l_i n_j \left[\frac{\dot{p}\delta_{ij} - \dot{\tau}_{ij}}{a_\infty r} + \frac{p\delta_{ij} - \tau_{ij}}{r^2}\right] dS(\mathbf{y}) \end{aligned} \tag{12}$$

Sarkar and Hussaini's form of the volume integral is retrieved when r becomes large. Equation (12) is one principal result of this paper.

3.2 Extension to 3D

Lighthill's equation, and hence Curle's solution, is valid in three dimensions, which means that the integrals have to be taken over a 3D volume and a 2D surface, respectively. For 2D cases, it is possible to derive a 2D analogue of equation (12), something that has been done by for example Gloerfelt *et al.*[23] The present work, however, will later move on to 3D geometries, and hence the 3D formulation of equation (12) is kept. Instead, 2D geometries will be viewed as infinite in the third direction, and the integrals will have to be extended in this direction. In other words, the two-dimensional field computed by the DS will be assumed to exist (and be identical) for all y_3, and the integrals will be taken over $-y_{3,ext} \leq y_3 \leq y_{3,ext}$ in the y_3 direction.

Note that this approach would have to be modified for turbulent flows: the two-dimensional field would then not be valid for all y_3. Instead, one could for example determine $y_{3,ext}$ so that the field is well correlated for $-y_{3,ext} \leq y_3 \leq y_{3,ext}$.

The 2D analogue of (12) is derived by use of the Green's function of the two-dimensional wave equation, which is a Hankel-function (as opposed to a Dirac δ-function in 3D). The existence of this 2D analogue is reassuring, since it means that the integrals will be convergent (i.e. the integrals will not go to infinity as $y_{3,ext} \to \infty$). Nevertheless, some numerical experimentation is needed to decide the cell size Δy_3 used to extend the integral in the third direction, and the distance $y_{3,ext}$ the integral is extended. Here, $\Delta y_3/D = 0.6$ and $y_{3,ext}/D = 180$ are found to generate errors less than 1%.

4 Results, Flow Field

4.1 Cavity Drag

The drag of the cavity per unit width (being a 2D geometry) is defined as

$$C_D = \frac{F_1}{\frac{1}{2}\rho_\infty U_\infty^2 D} \tag{13}$$

where F_1 is the force per unit width in the x_1-direction. After the initial transients have disappeared, a statistically stationary state is reached, as can be seen in figure 4(a). The mean drag is $\overline{C}_D = 0.384$, and it interesting to note that the drag associated with pressure alone (no viscous stress) is $\overline{C}_D^p = 0.409$, i.e. larger than the total drag. This is due to the fact that the flow along the bottom of the cavity is mainly towards the left, and hence the viscous contribution is actually to lower the drag. The values computed in this study are in qualitative agreement with other published results. Gharib and Roshko[9] report $\overline{C}_D \sim 0.3$ for the incompressible flow in axisymmetric cavities. Colonius *et al*[22] report $\overline{C}_D = 0.227$ for a similar case but at $M = 0.6$.

The spectrum of the cavity drag is plotted in figure 4(b), where the amplitude $\hat{C}_D$ of the drag is plotted versus the Strouhal number defined by

$$St_L = \frac{fL}{U_\infty} \tag{14}$$

The fundamental frequency is $St_L = 0.245$, and all higher modes are harmonics of this fundamental frequency. The first 4 modes are the largest, which means that most of the energy resides at $St_L \leq 1$. The results compare favourably with other published results. Colonius *et al*[22] report a fundamental frequency $St_L = 0.248$, which is almost identical to the value computed here. Other results worth mentioning are the ones by Ethembabaoglu,[11] who got $St_L \approx 0.5$ for the incompressible turbulent flow in a cavity with $L/D = 4$, and Shieh and Morris,[16] who got $St_L = 0.216$ in a cavity with $L/D = 4.4$ for $M = 0.6$ and turbulent flow.

4.2 Incoming Boundary Layer

Most studies on open cavity flows show the importance of the incoming boundary layer (BL), but few study it in more detail. An attempt at doing this is included here. Since the incoming BL in this study is laminar, the famous Blasius solution (see for example White[24]) is available for flat plate flows. Comparisons between the time-averaged BL in the simulation and the analytical solutions for a flat plate may yield some insight into open cavity flows.

The momentum thickness θ at the beginning of the resolved domain ($x_1/D = -4.3$) is used to compute the virtual origin of the BL, and this virtual origin is then used to determine the analytical solutions of the boundary layer parameters.[24]

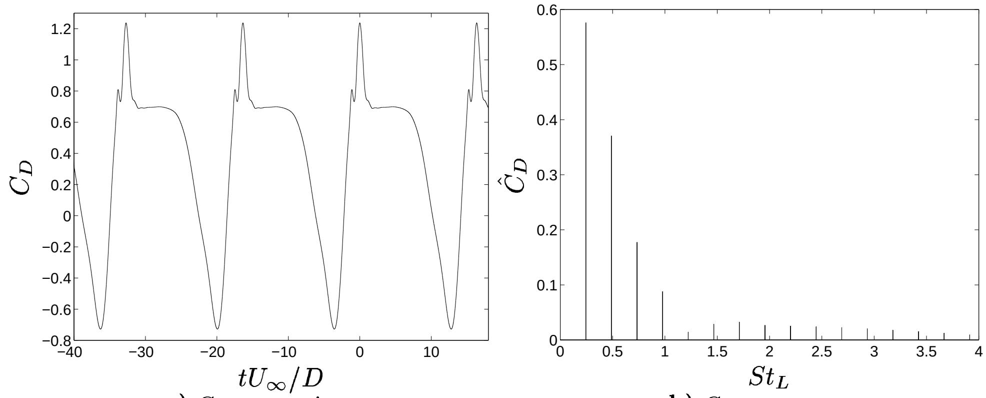

a) C_D versus time **b)** C_D spectrum

Fig. 4 Cavity drag

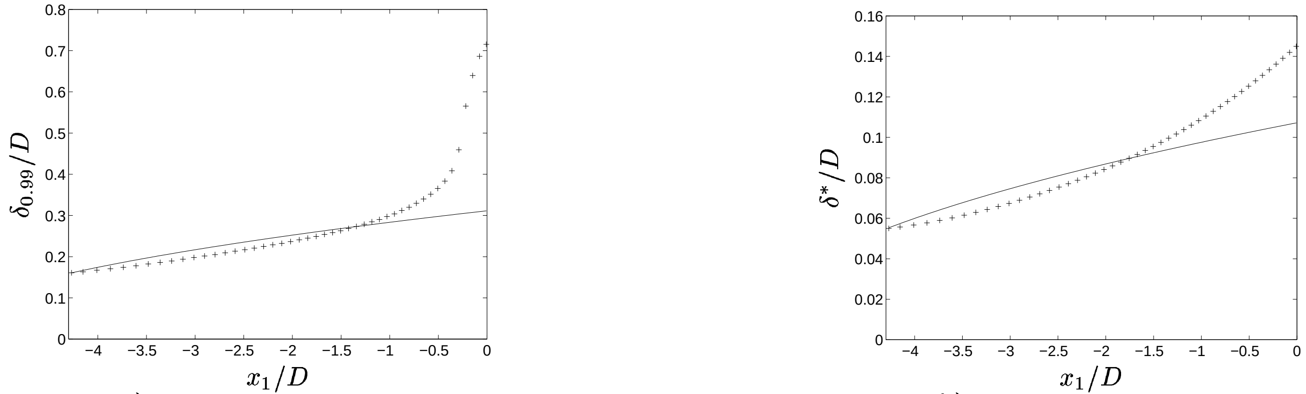

a) Boundary layer thickness **b)** Displacement thickness

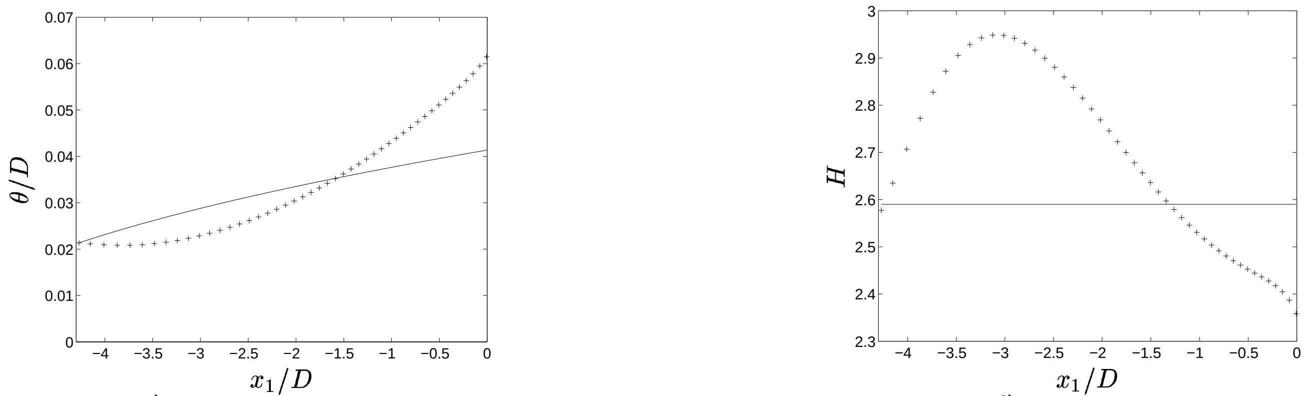

c) Momentum thickness **d)** Shape factor

Fig. 5 Incoming boundary layer. '-' analytical, '+' DS

The computed BL parameters are plotted in figure 5 together with the analytical solutions for a flat plate. It is seen that the time-averaged BL behaves in a very different way compared to a flat plate BL. The growth rate *increases* downstream, instead of *decreasing* like the flat plate solution. The plot of the momentum thickness is especially disturbing; since $\theta(x_1)$ is a measure of the drag from the virtual origin to x_1, figure 5(c) suggests that the plate drag up to $x_1/D \approx -3.8$ is negative, which it of course can not be. The problem here is that all these theories are based on a uniform freestream velocity U_∞, but the freestream velocity is actually increasing slowly with x_1 in this case. The reason is the periodic build-up and shedding of a vortex, which forces the freestream to accelerate around it.

The fact that the incoming BL behaves as it does complicates comparisons with other published investigations. Colonius *et al*,[22] for example, present the projected value of θ at the leading edge, assuming laminar growth. Other researchers, especially the experimentalists, present time-averaged values of $\delta_{0.99}$,

Parameter	Actual value	Projected value
$\delta_{0.99}/D$	0.715	0.311
δ^*/D	0.145	0.107
θ/D	0.0615	0.0413
H	2.36	2.59

Table 1 Incoming boundary layer parameters at $x_1 = 0$

δ^*, or θ at the leading edge. From the figures, it is clear that these measures can not be compared directly. The choice of Colonius *et al* is specifically cumbersome, since the projected values depend on how far upstream they are computed from. In this study, the projected and the actual parameters of the incoming BL are given in table 1.

4.3 Flow Features

The flow in open cavities is truly fascinating, with many complicated flow patterns despite the geometric simplicity. A sequence of snapshots with instantaneous streamlines are shown in figure 6.

The time has been defined to be $t \equiv 0$ at the peak in C_D (see figure 4(a)), and the period is $T_pU_\infty/D = 16.32$.

Starting at $tU_\infty/D = 12.24$, a vortex is formed at the leading edge. This vortex grows, and at $tU_\infty/D = 16.32$ a secondary vortex appears at the lower corner of the upstream cavity wall. At $tU_\infty/D = 2.04$, the primary vortex is large enough to deflect the flow above the cavity, and the boundary layer upstream of the cavity separates (albeit hard to see in the figures). At $tU_\infty/D = 8.16$, the secondary vortex (rotating counter-clockwise) has grown large enough to re-attach the upstream BL. At this time, the primary vortex has started to move downstream. At $tU_\infty/D = 10.20$, the primary vortex impinges on the downstream cavity wall, and during the next 2 snapshots it is ejected at the trailing edge. Freestream fluid is pulled down into the cavity at $tU_\infty/D = 14.28$, and it impinges on the downstream cavity wall at $tU_\infty/D = 16.32$, which is when the maximum drag occurs. The ejected vortices are convected along the wall downstream of the cavity until they leave the resolved domain.

The pressure coefficient c_p and the wall friction coefficient c_f are defined as

$$c_p = \frac{p - p_\infty}{\frac{1}{2}\rho_\infty U_\infty^2} \qquad (15)$$

and

$$c_{f,i} = \frac{n_j \tau_{ij}}{\frac{1}{2}\rho_\infty U_\infty^2} \qquad (16)$$

where $c_{f,i}$ is the friction coefficient in the i-direction. The mean values $\overline{c}_p$ and $\overline{c}_{f,i}$ are plotted in figure 7. The parameter s in the figures is the distance from the leading edge *along the wall*, and the vertical lines outline the corners of the cavity. The fact that the viscous contribution to the cavity drag is negative is now seen clearly, since $\overline{c}_{f,1}$ is mainly negative along the bottom wall. This, of course, is a result of the flow along the bottom being primarily to the left, as was seen in figure 6.

The mean pressure $\overline{c}_p$ is low on the upstream cavity wall and in the beginning of the cavity. It rises steeply towards the end of the cavity, and reaches a maximum in the lower, downstream wall, corner. This maximum is due to the periodic impingement of freestream fluid, which creates a stagnated region. The pressure decreases sharply at the trailing edge, due to the high acceleration around the edge. Behind the cavity, the pressure rises slowly and reaches a small peak at $x_1/D \approx 11$ (i.e. $s/D \approx 13$), from where it falls of.

$\overline{c}_p$ along the bottom wall from Shieh and Morris[16] is included in figure 7(a). Despite being a different case ($L/D = 4.4$, $M = 0.6$, $Re = 200000$, $\delta_{0.99}/D = 0.2$), the mean pressure coefficients are remarkably similar. Note that their results were for a longer cavity, and hence their bottom wall extends to $s/D = 5.4$. The trends are very similar: a minimum at $x_1/D \approx 1$ followed by a steep increase as the downstream cavity wall is approached. Shieh and Morris got a larger maximum value of $\overline{c}_p$ at the downstream cavity wall, which could be a result of their longer cavity, giving the flow a larger distance for pressure recovery. This hypothesis is strengthened by the fact that the profiles follow the same trend between $x_1/D \approx 2$ and $x_1/D \approx 3.5$. Another possibility is that the higher Mach number of Shieh and Morris' case gives higher 'oscillations', an idea that is emboldened by the fact that all peaks are stronger in their results. A last possibility is the fact that their results were computed using a turbulence model, which could have given erroneous results.

The small peak of $\overline{c}_p$ at $x_1/D \approx 11$ is probably an effect of a small secondary vortex. This smaller vortex is only seen in figure 6 as a small disturbance of the primary vortex as it travels downstream from the cavity. At $x_1/D \approx 11$ ($s/D \approx 13$, figure 6(c)), the smaller vortex is located in the lower part of the primary vortex, and this may enhance the entrainment of fluid towards the wall. This would then increase the pressure on the wall at that location.

5 Results, Radiated Sound

One of the objectives listed in section 1.1 is to analyze the acoustic noise generation in detail, which is an area that has received remarkably little attention, at least in computational studies, judging from published work. Among the few investigations dealing in detail with the sources of sound, Freund's[25] study of the noise sources in a jet, and Mankbadi *et al*'s[26] investigation of supersonic jet noise, are two examples.

5.1 Contributing Source Terms

Curle's equation is linear, and hence the contributions from the various source terms can be computed

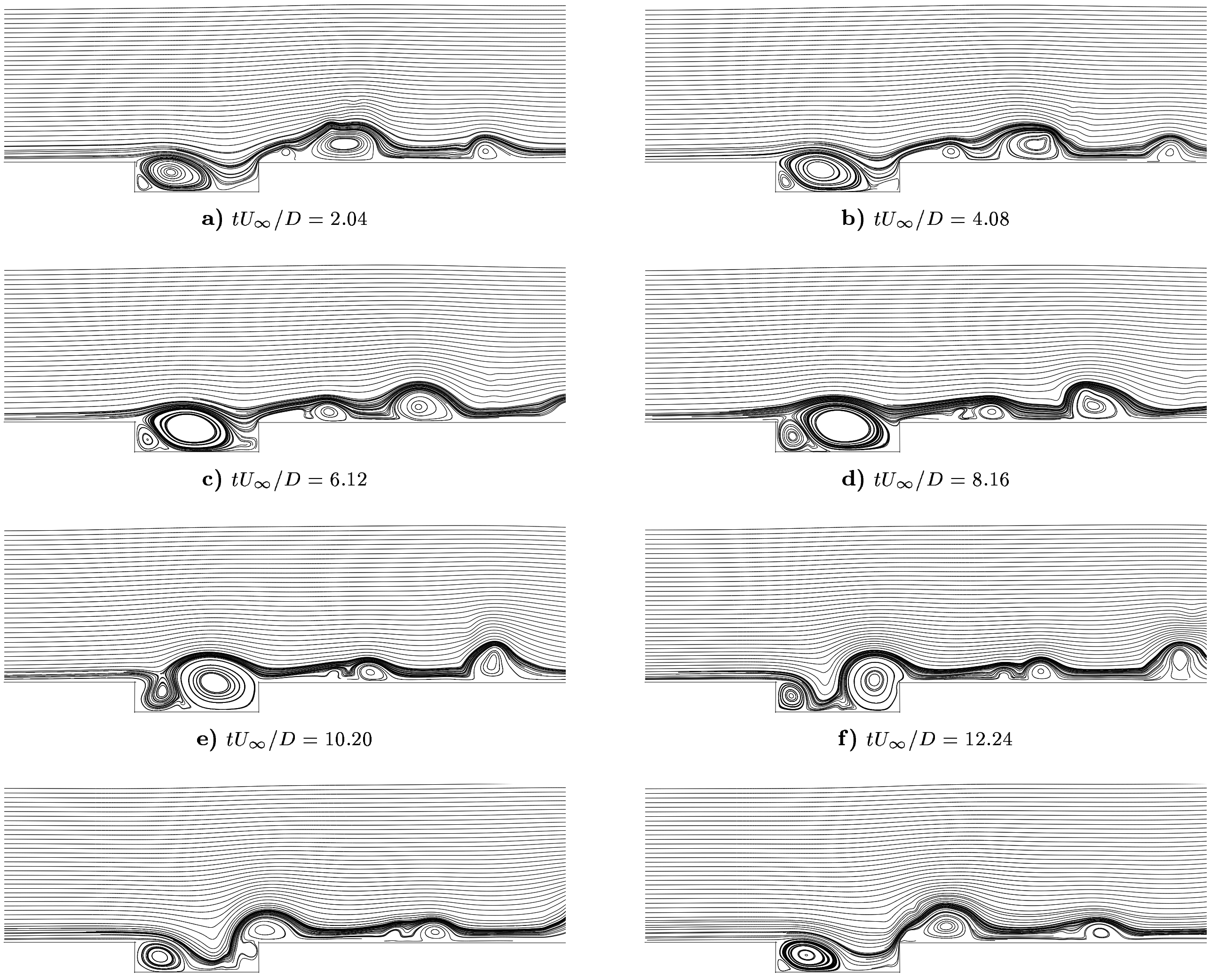

a) $tU_\infty/D = 2.04$ **b)** $tU_\infty/D = 4.08$

c) $tU_\infty/D = 6.12$ **d)** $tU_\infty/D = 8.16$

e) $tU_\infty/D = 10.20$ **f)** $tU_\infty/D = 12.24$

g) $tU_\infty/D = 14.28$ **h)** $tU_\infty/D = 16.32$

Fig. 6 Instantaneous streamlines

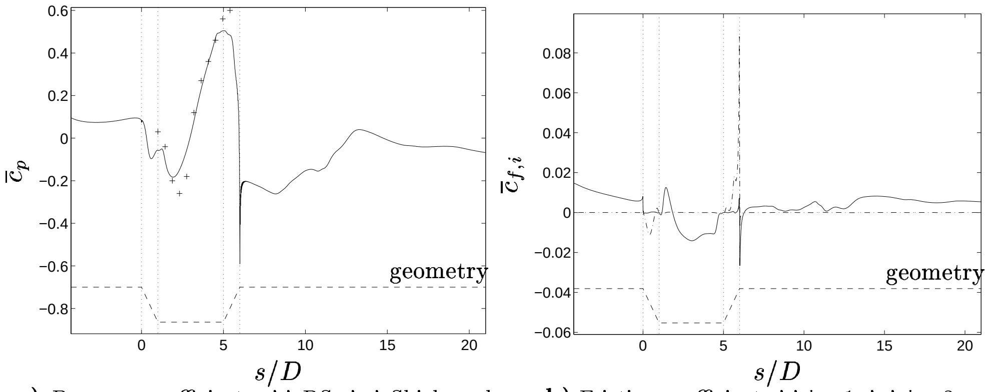

a) Pressure coefficient. '-' DS, '+' Shieh and Morris[16] **b)** Friction coefficient. '-' $i = 1$, '-.' $i = 2$

Fig. 7 Mean pressure and friction coefficients

independently. It is considered 'common knowledge' in the community of aero acoustic researchers, that pressure fluctuations on solid walls will be the primary sources of sound at low Mach numbers, and also that Lighthill's tensor T_{ij} can be simplified to $T_{ij} \approx \rho_\infty u_i u_j$ for most flows, but to the knowledge of this author, no one has actually presented quantitative proof that this is the case. Even if one agrees with the dimensional arguments put forth by Lighthill,[1] Curle,[5] and others, justifying the facts mentioned above, a quantitative

Number	Term	$\overline{I}/\overline{I}_{ds}$
1	$\partial p/\partial \tau\|_w$	0.46
2	$p\|_w$	0.37
3	$\partial \tau_{ij}/\partial \tau\|_w$	$3.5 \cdot 10^{-7}$
4	$\tau_{ij}\|_w$	$6.9 \cdot 10^{-7}$
5	$\partial^2 \rho_\infty u_i u_j/\partial \tau^2$	0.056
6	$\partial^2 (\rho - \rho_\infty) u_i u_j/\partial \tau^2$	$2.4 \cdot 10^{-5}$
7	$\partial^2 \tau_{ij}/\partial \tau^2$	$\sim 10^{-7}$
8	$\partial^2 (p - a_\infty^2 \rho)\delta_{ij}/\partial \tau^2$	$5.0 \cdot 10^{-4}$
9	$\partial \rho_\infty u_i u_j/\partial \tau$	0.068
10	$\rho_\infty u_i u_j$	0.045

Table 2 Contributions from different source terms

analysis might generate further insight into aerodynamic sound generation.

Curle's equation in its modified form (12) involves a total of 13 source terms: 9 in the volume ($\ddot{T}_{ij}$, $\dot{T}_{ij}$, and T_{ij}, where each consists of $\rho u_i u_j$, τ_{ij}, and $(p - a_\infty^2 \rho)\delta_{ij}$), and 4 on the walls ($\dot{p}$, $\dot{\tau}_{ij}$, p, and τ_{ij}). Furthermore, since the common simplification of T_{ij} introduces ρ_∞, Lighthill's tensor is best written $T_{ij} = \rho_\infty u_i u_j + (\rho - \rho_\infty) u_i u_j - \tau_{ij} + (p - a_\infty^2 \rho)\delta_{ij}$, bringing the total number of source terms to 16.

In order to analyze the contribution of each source term, the radiated sound at an observer located at $\mathbf{x}/D = (1, 7.16)$ is computed by Curle's equation. The sound intensity of each contribution is then computed by[27]

$$\overline{I} = \frac{\overline{(p')^2}}{\rho_\infty a_\infty} \tag{17}$$

The results, scaled with the intensity computed at the same observer from the DS, are presented in table 2. As can be seen in the table, the viscous terms (terms 3, 4, and 7) are negligible, both on the walls and in the volume. The assumption of $\rho \approx \rho_\infty$ introduces a very small error (term 6), and the entropy term (term 8) is negligible as well. Due to these findings, the first and zeroth order temporal derivatives of the viscous, entropy, and $(\rho - \rho_\infty) u_i u_j$ terms are skipped and not included in the table.

The contributions of the volume terms (terms 5, 9, and 10) are about 10-15% of the wall term contributions (terms 1 and 2). A comparison like this one, however, does not take any cancellation effects into account (i.e. it ignores phase information). To analyze the contributions further, the pressure signals are plotted versus time in figure 8.

Figure 8(a) shows the contributions of terms 1 and 2, as well as the sum of them. Note that some signals have been offset (moved down) slightly for clarity. The sum is very promising, since it shows remarkable similarity to the signal computed in the DS. From the individual contributions, it is seen that terms 1 and 2 are roughly equally important (as indicated in table 2), and that there exists a phase lag between terms 1 and 2 at the main peaks.

Observer	x_1/D	x_2/D
1	-2	7.16
2	-1	7.16
3	0	7.16
4	1	7.16
5	2	7.16
6	3	7.16
7	4	7.16
8	5	7.16
9	6	7.16

Table 3 Observer locations

Figure 8(b) shows the total contribution of both wall and volume terms. When compared to the results from the wall terms alone, the agreement between the signals computed by Curle's equation and the DS is better around $tU_\infty/D \approx 5$, but worse around $tU_\infty/D \approx 14$. The sharp oscillations around $tU_\infty/D \approx 14$ indicate that the resolution (when computing the integral, i.e. the number of samples) perhaps should have been higher in time.

So which terms are important in Curle's equation? The wall pressure terms (1 and 2) are dominant, and account for most of the radiated sound, whereas the simplified volume terms (5, 9, and 10) only modify the signal slightly. Whether the volume terms are important in terms of the radiated intensity, will be analyzed in section 5.2.

5.2 Radiated Sound

The radiated sound to the observers, listed in table 3 (see also figure 1), is computed by Curle's modified equation (12). Points 1, 2, 8, and 9 are located in positions where they are shielded from parts of the source regions, which in a way illustrates one of the weaknesses of the scalar methods. In this study, those parts of the walls that are blocked from view from the observer, are excluded in Curle's integral, but the volume integral is taken over the whole domain. Albeit wrong, this is done for simplicity. The error introduced should be fairly small, since these shielded regions are small.

The Overall Sound Pressure Levels ($OASPL$), defined as[7]

$$OASPL = 20 \log_{10} \left(\frac{p_{rms}}{p_{ref}} \right) \tag{18}$$

with $p_{ref} = \sqrt{\rho_\infty a_\infty 10^{-12} W/m^2}$, computed by the wall pressure contribution in Curle's equation is plotted in figure 9(a), and it is seen that the levels are under-predicted by between 0.3 and 2.7 dB. The shape of the directivity is in fairly good agreement with the DS, but the under-prediction is larger straight above the downstream wall. The reason to this is not known, but it is hypothesized that it may be due to either the lack of mean flow convection (which would enhance the downstream radiation), or the fact that the do-

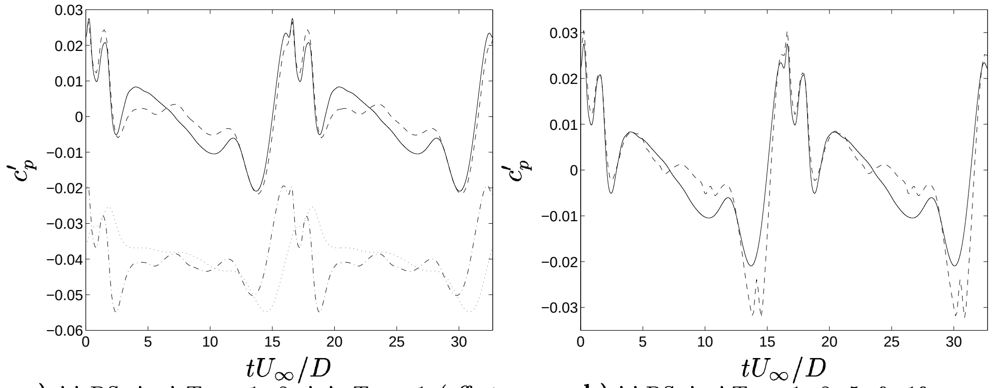

a) '-' DS, '- -' Term 1+2, '-.' Term 1 (offset -0.04), ':' Term 2 (offset -0.04)

b) '-' DS, '- -' Term 1+2+5+9+10

Fig. 8 Radiated pressure signals at $\mathbf{x}/D = (1, 7.16)$

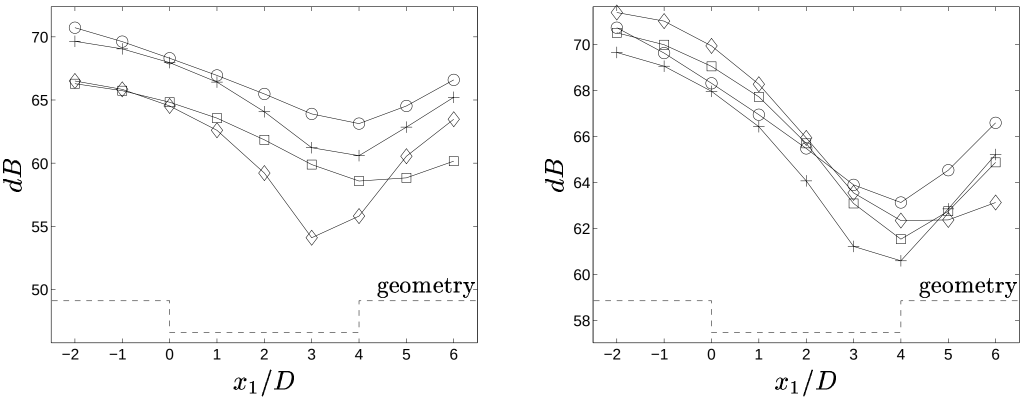

a) 'o' DS, '+' Term 1+2, '□' Term 1, '◇' Term 2

b) 'o' DS, '+' Term 1+2, '□' Term 1+2+5, '◇' Term 1+2+5+9+10

Fig. 9 Overall Sound Pressure Levels at 9 observers

main may be too short downstream. Looking at the individual contributions, the p/r^2 part (term 2) shows the strongest directivity. Since this term disappears in the far field, the directivity will be flatter at larger distances.

The radiated sound intensity when the volume terms are added is plotted in figure 9(b). Addition of term 5 improves the agreement slightly, and the maximum error is decreased to about 1.8 dB. The full contribution, including all dominant wall and volume terms, makes the agreement slightly worse. The over-prediction upstream is increased, as well as the under-prediction downstream. The maximum error is increased to 3.5 dB.

Since the errors in the Direct Simulation were estimated to be smaller than 3.6 dB in section 2.4, it is hard to quantify the accuracy of Curle's equation. All combinations of source terms in figure 9, however, give results that are qualitatively correct, and within the error margin in the DS.

6 Wall Sources

The strength of the acoustic sources is defined here as

$$S_l \equiv 20 \log_{10} \frac{\Phi_{l,rms}}{\Phi_{l,ref}} \qquad (19)$$

where Φ_l is one of the source terms listed in table 2. With this scaling, an increase of 10 dB is equivalent to a 10-fold increase in intensity, and an increase of 3 dB means a doubling of the intensity. $\Phi_{l,ref}$ acts only to change the level of the source strength, so, as long as only *relative* information is of interest, it can be chosen arbitrarily. Here, the reference for the wall pressure fluctuation ($l = 2$) is chosen to be the same as that for the $OASPL$ of the radiated sound, i.e. $\Phi_{2,ref} = p_{ref} = \sqrt{\rho_\infty a_\infty 10^{-12} W/m^2}$. This choice means that S_2 is the $OASPL$ at the wall. Since terms 1 and 3 involve temporal derivatives, a factor U_∞/D is included in $\Phi_{l,ref}$ as, for example, $\Phi_{1,ref} = p_{ref} U_\infty/D$.

6.1 Pressure Sources

The strengths of the wall pressure sources (S_1 and S_2) are plotted in figure 10(a). They are small at the

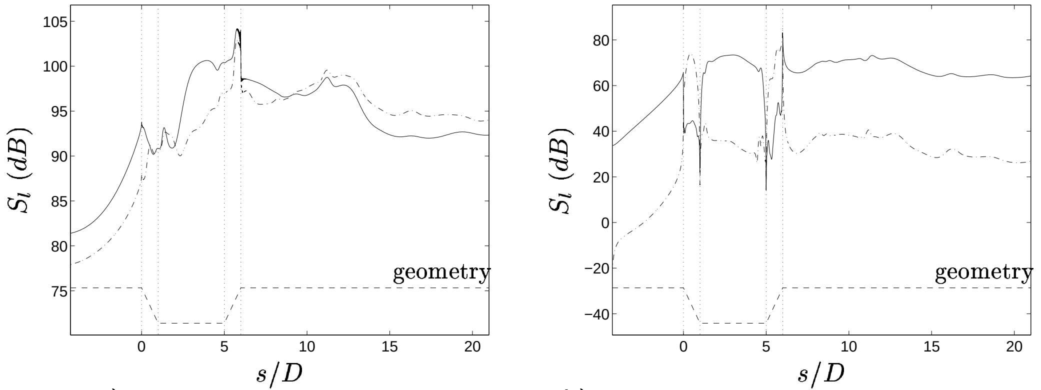

a) Pressure terms. '-' S_2, '-.' S_1 **b)** Viscous terms. '-' S_4 $(n_j\tau_{1j})$, '-.' S_4 $(n_j\tau_{2j})$

Fig. 10 Wall source strengths

inlet, and grow a about a factor of 10 as they approach the leading edge. The low levels at the inlet are explained by the fact that the boundary layer is laminar, and the increase closer to the leading edge is due to the periodic separation of the BL upstream of the leading edge. The sources grow even larger towards the end of the bottom cavity wall, and reach a peak at the upper part of the downstream cavity wall. After the cavity, they stay fairly constant until $x_1/D \approx 11$ (i.e. $s/D \approx 13$), where they drop about 3-5 dB. This drop occurs at the same location where $\overline{c}_p$ was found to have a small peak in figure 7(a), and where the small vortex was found in figure 6.

The fact that the contributions of terms 1 and 2 were found to be of similar magnitude in section 5.1 is, of course, not a coincidence. Assuming that terms 1 and 2 are affected similarly by cancellations, the radiated intensities would scale as

$$\frac{\overline{I}_2}{\overline{I}_1} \sim \frac{\overline{\left(\frac{Ap'}{r^2}\right)^2}}{\left(\frac{A}{a_\infty r}\frac{\partial p}{\partial \tau}\right)^2} \sim \frac{a_\infty^2}{r^2}\frac{p_{rms}^2}{(\dot{p})_{rms}^2} \tag{20}$$

where A is some sound radiating area. Equation (19) is used to write

$$\begin{aligned} p_{rms}^2 &= p_{ref}^2\, 10^{S_2/10} \\ (\dot{p})_{rms}^2 &= \frac{U_\infty^2\, p_{ref}^2}{D^2}\, 10^{S_1/10} \end{aligned} \tag{21}$$

which yields

$$\frac{\overline{I}_2}{\overline{I}_1} \sim \frac{a_\infty^2}{r^2}\frac{D^2\, 10^{S_2/10}}{U_\infty^2\, 10^{S_1/10}} \sim \frac{1}{M^2\,(r/D)^2} 10^{(S_2-S_1)/10} \tag{22}$$

In this case, with $M = 0.15$, $r/D \approx 8$ (measured from the end of the cavity to the observer), and $S_1 \sim S_2$, the ratio would be $\overline{I}_2/\overline{I}_1 \approx 0.7$. This is, at least qualitatively, in agreement with the results in table 2, and can be taken as an indication that the contributions from terms 1 and 2 are, indeed, affected by cancellations similarly.

The region between $x_1/D \approx 2$ and $x_1/D \approx 11$ is where most of the sound generation takes place, with the downstream cavity wall making the primary contribution. This fact will later be used to explain the directivity of sound from the cavity.

6.2 Viscous Sources

The viscous source strength S_4 is plotted in figure 10(b). The corresponding plot for S_3 is omitted, partly because of the unimportance of the viscous contribution, and partly because S_3 and S_4 look remarkably similar. As expected, the viscous sources are strongest *along* the wall (as opposed to normal to the wall). The levels are about 25 dB (a factor 1/300) lower than for the pressure sources. Following the arguments above, the viscous contribution to the sound intensity at $\mathbf{x}/D = (1, 7.16)$ should then be about 1/300 of the contributions from the pressure sources. Table 2, on the other hand, shows the viscous contribution to be about 10^{-6} of that of the pressure. How can this discrepancy be explained?

The critical point here is the fact that the viscous source strength is large *along* the wall. Since the area radiating to an observer is large when the observer is located nearly normal to the wall, but small when the observer is located nearly tangential to the wall, it is clear that the viscous source strength *normal* to the wall is more relevant in a comparison. The normal source strength is about 65 dB lower than the pressure strength, which corresponds to about 10^{-6} lower intensity.

6.3 Correlations

In an attempt to gain further insight into the acoustics of the open cavity, the sound signals at the observers (taken from the DS) are correlated with the dominating sources on the wall, taking the retarded time into account.

The correlation $R_l(\mathbf{x}, \mathbf{y})$ is defined as

$$R_l(\mathbf{x},\mathbf{y}) \equiv \frac{\overline{p(\mathbf{x},t)\Phi_l(\mathbf{y}, t - r/a_\infty)}}{p_{rms}(\mathbf{x})\Phi_{l,rms}(\mathbf{y})} \tag{23}$$

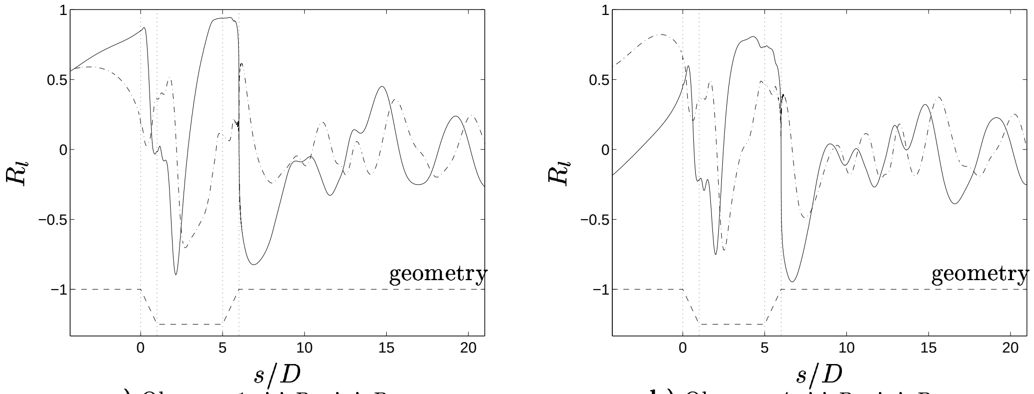

a) Observer 1. '-' R_2, '-.' R_1 **b)** Observer 4. '-' R_2, '-.' R_1

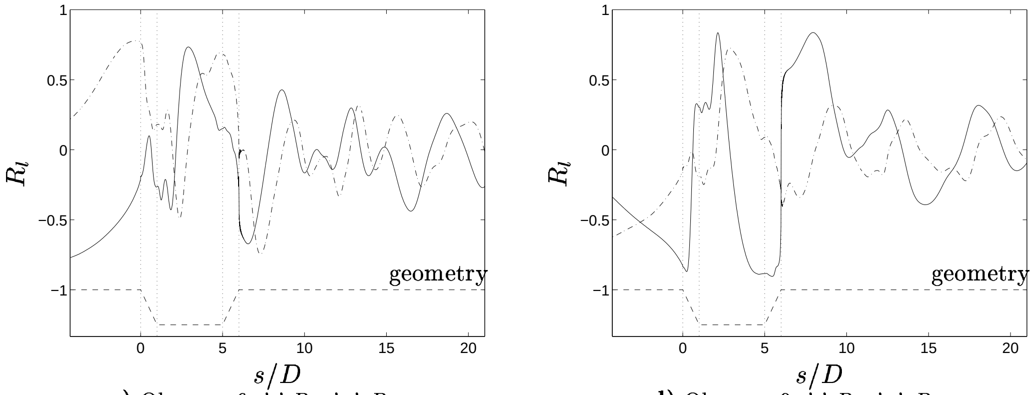

c) Observer 6. '-' R_2, '-.' R_1 **d)** Observer 9. '-' R_2, '-.' R_1

Fig. 11 Correlations between radiated sound and wall source terms

where $p(\mathbf{x}, t)$ is the pressure signal at an observer location, $\Phi_l(\mathbf{y}, t - r/a_\infty)$ is a source term at a source location, the bar denotes a temporal average, and $r = |\mathbf{x} - \mathbf{y}|$. The correlations for some observers are plotted in figure 11.

Before analyzing the correlations, some thought on what the correlation actually means is necessary. A high value of $R_l(\mathbf{x}, \mathbf{y})$ means that the signals have similar shapes and phases, which in this case means that the source has acted constructively (or increased the amplitude). $R_l(\mathbf{x}, \mathbf{y}) < 0$, on the other hand, means that the source has acted destructively and decreased the amplitude of the radiated signal. Whether the source has made a significant contribution or not can not be determined from the correlation; instead, the source strength in figure 10 has to be taken in consideration.

Regardless of observation location, the correlations oscillate around 0 above $x_1/D \approx 9$ (i.e. $s/D \approx 11$). This is an effect of the vortices being convected along the wall, generating pressure fluctuations as they pass each point on the wall. Since the length scale of these pressure fluctuations is much shorter than the acoustic length scales, the contributions will change from constructive to destructive and back again for different points along the wall. The drop in source strength occurs at $x_1/D \approx 11$ (see figure 10), so the sources above, say, $x_1/D \approx 11$ will probably not contribute significantly to the radiated sound.

Another interesting observation is the 'spatial phase difference' between R_1 and R_2; it is an effect of the temporal phase difference between $\dot{p}$ and p (differentiation of a signal with respect to time changes the phase $\pi/2$). Since R_1 and R_2 have different shapes, the radiated sound in the far field will be different from that in the near field, being dominated by the sound generation in different regions.

In general, R_2 changes more between different observation locations than R_1 does. An example of this is the region $x \leq 0$, where R_1 is positive for observers 1, 4, and 6, but where R_2 changes from positive to negative for the same observers. The reason to this is not known.

6.4 Directivity

The directivity pattern, specifically the increased radiation at upstream locations, is easier to understand in the framework of Curle's equation than directly from the DS. In Direct Simulations, there is no way of telling where the sound originated from, but when using a scalar equation this becomes possible.

The contribution from a wall pressure source includes a term $l_i n_i = \cos\varphi$, where φ is the angle between the wall normal and the direction to the observer. Due to this, and the geometry of the cavity, it is clear that the contribution from the downstream cavity wall grows larger upstream. Figure 10(a) shows that the strongest source, S_2, has its peak at the downstream cavity wall, which then explains the increased radiation in the upstream direction. The fact that the correlation R_2 at the downstream cavity wall is very high for observer 1, and becomes successively lower for observers 2 to 6, confirms this.

Since R_2 is higher than R_1 for observers 1 to 5, and especially so for the observers farthest upstream, the main contribution to the radiated sound at those observers is that of term 2. Since the contribution from term 2 will disappear at larger distances (due to the $1/r^2$ factor), and since S_1 has a less pronounced maximum at the downstream cavity wall in figure 10(a), the upstream dominance is expected to decrease in the far field. This is confirmed by figure 9(a), in which the directivity is seen to be flatter for the $\partial p/\partial t$-term.

A similar argument can be made for the downstream radiation in the far field. Figure 11(d) shows that term 2 (R_2) is the main contribution to the sound at observer 9, whereas R_1 is smaller. This indicates that the directivity downstream, as well as upstream, will be flatter farther away from the cavity.

6.5 Volume Sources

The source strength of the volume sources is defined exactly as for the wall sources, i.e. by equation (19). The reference value is defined in a similar way, so, for example, $\Phi_{5,ref} = p_{ref}(U_\infty/D)^2$.

The source strengths of the volume sources are plotted in figures 12, 13, and 14. The volume source terms, especially S_5 (figure 12), have their maximums right behind the cavity. When comparing with the instantaneous flow field in figure 6, it is seen that the region of maximum S_5 is located slightly above the path of the vortices ejected from the cavity. The fact that the source strength is comparatively smaller *in* the cavity is a somewhat surprising result; after all, that is the region where the violent ejection of the vortices originates. The explanation could perhaps be that the flow field in the cavity is built up relatively slowly, whereas it changes more quickly in the region into which the vortices are ejected. This explanation is supported by the fact that the lower order temporal derivatives of T_{ij} (S_9 and S_{10}) have less pronounced maximums in this region.

Knowing that the volume sources have their maximums behind the cavity, it is somewhat surprising that the main contribution from the volume sources is for the *upstream* observers, as shown in figure 9(b). The reason for this must be that the volume sources are out of phase with the wall sources, and hence they interact destructively downstream. At higher Mach numbers, the volume sources are expected to be more important, and hence the upstream dominance may disappear. That being said, higher Mach numbers would increase the effects of mean convection, an effect excluded from Curle's equation, which may make these arguments invalid.

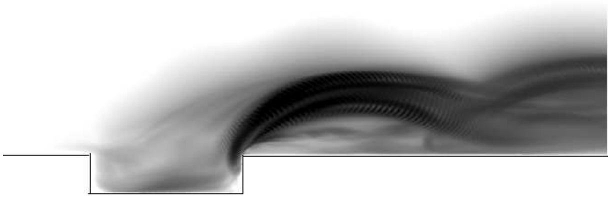

a) $\ddot{T}_{11}$

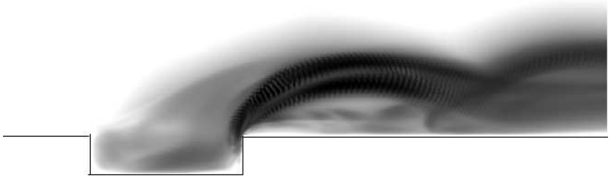

b) $\ddot{T}_{12}$

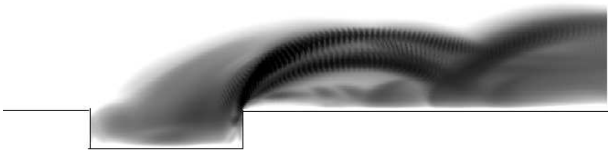

c) $\ddot{T}_{22}$

Fig. 12 Volume source strength, S_5. grayscale between 60 dB and 120 dB.

Some numerical, high-wave number, oscillations are present in figure 12, but not as much in the other 2 figures. That the $\ddot{T}_{ij}$ term is especially affected by these grid to grid oscillations is not surprising, since the temporal derivatives enhance higher frequencies. Whether these numerical oscillations have an effect on the radiated sound, and if so, how big it is, is not known. They could be removed by increasing the artificial dissipation, but that would affect the accuracy of the DS adversely.

7 Summary

The more general findings of this study can be summarized as:

- The solution of Curle's equation has been written on a form with temporal derivatives, while still being valid in the near field.
- The main sources of sound in a low Mach number, wall bounded, flow are the pressure fluctuations on the walls. The viscous contribution on the walls is found negligible, since it mainly acts *along* the walls. The sources in the fluid are small, about 10% of the wall sources for this particular case.

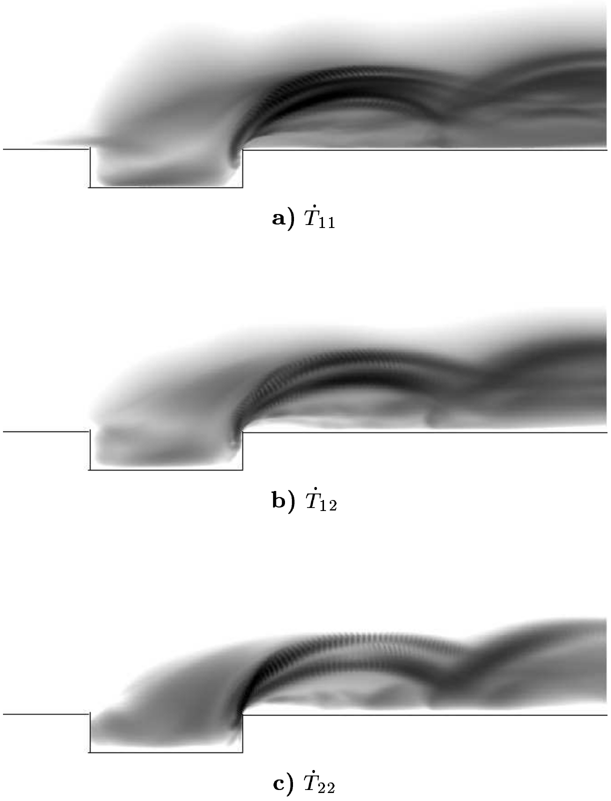

a) $\dot{T}_{11}$

b) $\dot{T}_{12}$

c) $\dot{T}_{22}$

Fig. 13 Volume source strength, S_9. grayscale between 60 dB and 100 dB.

- The common simplification of Lighthill's tensor $T_{ij} \approx \rho_\infty u_i u_j$ is valid, and introduces very small errors at low Mach numbers.

- Being mainly effects of hydrodynamics, the main source terms *should* be computable from the incompressible equations, but this has not been investigated in this study.

- The tool of correlations can yield further insight into aero acoustic noise generation.

- A Direct Simulation is very sensitive to the boundary conditions. The boundary conditions, coupled with the domain size, used in this study are adequate, but should be improved.

- Curle's equation is, at least in the near field, sensitive to the size of the domain over which the source terms are integrated. This sensitivity, however, is smaller than the sensitivity to boundary conditions of the Direct Simulation.

The findings on the open cavity are:

- The sources of sound are largest on the downstream cavity wall. They are also large along the second half of the bottom of the cavity, and about 2 cavity lengths behind the cavity.

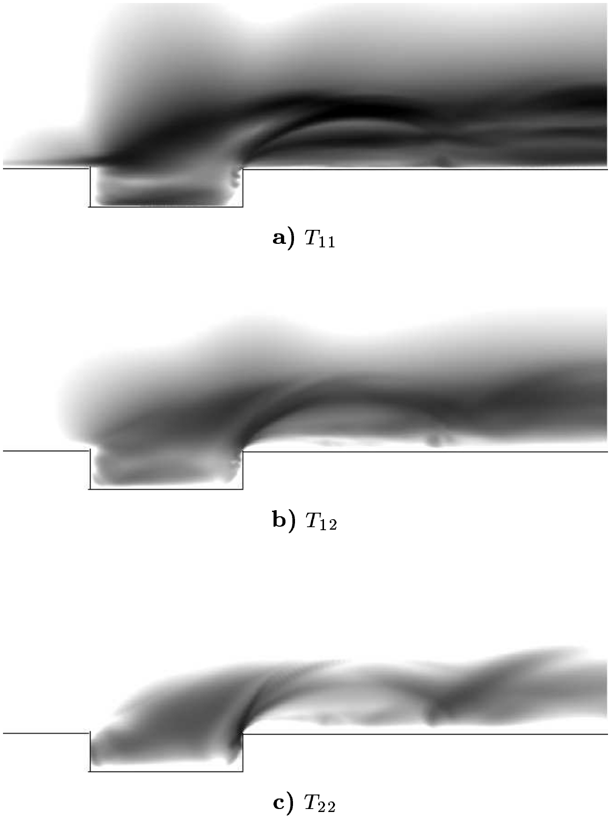

a) T_{11}

b) T_{12}

c) T_{22}

Fig. 14 Volume source strength, S_{10}. grayscale between 60 dB and 90 dB.

- The directivity of the radiated sound is explained by noting that the regions of high source strength contribute primarily to the upstream and downstream directions.

- Correlations between the source terms and the radiated sound show that the directivity will be flatter in the far field.

- The incoming boundary layer behaves nothing like a flat plate boundary layer. A consequence of this is that it is hard to specify the boundary layer characteristics in a non-ambiguous way.

- The sound sources in the fluid, albeit small, are large primarily *behind* the cavity.

8 Acknowledgements

This work was supported by Volvo Car Corporation and the Swedish Agency for Innovation Systems (VINNOVA).

References

[1] Lighthill, M. J., "On Sound Generated Aerodynamically, I. General Theory," *Proc. Roy. Soc.*, Vol. A 211, 1952, pp. 564–587.

[2] Phillips, O. M., "On the Generation of Sound by Supersonic Turbulent Shear Layers," *Journal of Fluid Mechanics*, Vol. 9, 1960, pp. 1–27.

[3] Lilley, G. M., "On the Noise from Jets," *AGARD CP-131*, 1974.

[4] Doak, P. E., "Analysis of Internally Generated Sound in Continuous Materials: 2. A Critical Review of the Conceptual Adequacy and Physical Scope of Existing Theories of Aerodynamic Noise, with Special Reference to Supersonic Jet Noise," *Journal of Sound and Vibration*, Vol. 25, 1972, pp. 263–335.

[5] Curle, N., "The Influence of Solid Boundaries Upon Aerodynamic Sound," *Proc. Roy. Soc.*, Vol. A 231, 1955, pp. 505–514.

[6] Ffowcs Williams, J. E. and Hawkins, D. L., "Sound Generation by Turbulence and Surfaces in Arbitrary Motion," *Philos. Trans. Roy. Soc.*, Vol. A 264 No. 1151, 1969, pp. 321–342.

[7] Larsson, J., "Computational Aero Acoustics for Vehicle Applications," Licentiate thesis, Chalmers University of Technology, 2002.

[8] Sarkar, S. and Hussaini, M. Y., "Computation of the Acoustic Radiation from Bounded Homogeneous Flows," *Computational Aero Acoustics*, 1993, pp. 335–354.

[9] Gharib, M. and Roshko, A., "The Effect of Flow Oscillations on Cavity Drag," *Journal of Fluid Mechanics*, Vol. 177, 1987, pp. 501–530.

[10] Rockwell, D. and Naudascher, E., "Review - Self-Sustaining Oscillations of Flow Past Cavities," *Journal of Fluids Engineering*, Vol. 100, 1978, pp. 152–165.

[11] Ethembabaoglu, S., "On the Fluctuating Flow Characteristics in the Vicinity of Gate Slots," Tech. rep., University of Trondheim, Norwegian Institute of Technology, 1973.

[12] Sarohia, V., "Experimental Investigation of Oscillations in Flows Over Shallow Cavities," *AIAA Journal*, Vol. 15, 1977, pp. 984–991.

[13] Rossiter, J. E., "Wind Tunnel Experiments on the Flow Over Rectangular Cavities at Subsonic and Transonic Speeds," Technical report 3438, Aeronautical Research Council Reports and Memoranda, 1964.

[14] Ahuja, K. K. and Mendoza, J., "Effects of Cavity Dimensions, Boundary Layer, and Temperature on Cavity Noise with Emphasis on Benchmark Data to Validate Computational Aeroacoustic Codes," *NASA*, Vol. CR-4653, 1995.

[15] Colonius, T., Lele, S. K., and Moin, P., "Boundary Conditions for Direct Computation of Aerodynamic Sound Generation," *AIAA Journal*, Vol. 31 No. 9, 1993, pp. 1574 - 1582.

[16] Shieh, C. M. and Morris, P. J., "Parallel Computational Aeroacoustic Simulation of Turbulent Subsonic Cavity Flow," *AIAA*, Vol. 2000-1914, 2000.

[17] Ashcroft, G. and Zhang, X., "A Computational Investigation of the Noise Radiated by Flow-Induced Cavity Oscillations," *AIAA*, Vol. 2001-0512, 2001.

[18] Eriksson, L.-E., "Development and Validation of Highly Modular Flow Solver Versions in g2dflow and g3dflow," Internal report 9970-1162, Volvo Aero Corporation, 1995.

[19] Billson, M., "Computational Techniques for Jet Noise Predictions," Licentiate thesis, Chalmers University of Technology, 2002.

[20] Billson, M., Eriksson, L.-E., and Davidson, L., "Acoustic Source Terms for the Linear Euler Equations on Conservative Form," *AIAA*, Vol. 2002-2582, 2002.

[21] Tam, C. K. W. and Webb, J. C., "Dispersion-Relation-Preserving Finite Difference Schemes for Computational Acoustics," *Journal of Comp. Physics*, Vol. 107, 1993, pp. 262–281.

[22] Colonius, T., Basu, A. J., and Rowley, C. W., "Computation of Sound Generation and Flow/Acoustic Instabilities in the Flow Past an Open Cavity," *3rd ASME/JSME Joint Fluids Engineering Conference*, Vol. FEDSM99-7228, 1999.

[23] Gloerfelt, X., Bailly, C., and Juvé, D., "Computation of the Noise Radiated by a Subsonic Cavity Using Direct Simulation and Acoustic Analogy," *AIAA*, Vol. 2001-2226, 2001.

[24] White, F. M., *Fluid Mechanics, 3rd Edition*, McGraw-Hill, 1994.

[25] Freund, J. B., "Noise Sources in a Low-Reynolds-Number Turbulent Jet at Mach 0.9," *Journal of Fluid Mechanics*, Vol. 438, 2001, pp. 277–305.

[26] Mankbadi, R. R., Hayer, M. E., and Povinelli, L. A., "Structure of Supersonic Jet Flow and Its Radiated Sound," *AIAA Journal*, Vol. 32 No. 5, 1994, pp. 897–906.

[27] Pierce, A. D., *Acoustics. An Introduction to Its Physical Principles and Applications*, Acoustical Society of America, Woodbury, New York, 1991.